PHYSICS

Injection-free multiwavelength electroluminescence devices based on monolayer semiconductors driven by an alternating field

Jiabin Feng[1,2,3]†, Yongzhuo Li[1,2,3]†, Jianxing Zhang[1,2,3], Yuqian Tang[1,2,3], Hao Sun[1,2,3], Lin Gan[1,2,3], Cun-Zheng Ning[1,2,3,4]*

Two-dimensional (2D) semiconductors have emerged as promising candidates for various optoelectronic devices especially electroluminescent (EL) devices. However, progress has been hampered by many challenges including metal contacts and injection, transport, and confinement of carriers due to small sizes of materials and the lack of proper double heterostructures. Here, we propose and demonstrate an alternative approach to conventional current injection devices. We take advantage of large exciton binding energies in 2D materials using impact generation of excitons through an alternating electric field, without requiring metal contacts to 2D materials. The conversion efficiency, defined as the ratio of the emitted photons to the preexisting carriers, can reach 16% at room temperature. In addition, we demonstrate the first multiwavelength 2D EL device, simultaneously operating at three wavelengths from red to near-infrared. Our approach provides an alternative to conventional current-based devices and could unleash the great potential of 2D materials for EL devices.

INTRODUCTION

Two-dimensional (2D) layered semiconductors such as transition metal dichalcogenides (TMDCs) or black phosphorus have attracted a great deal of attention since the first demonstration of indirect-to-direct bandgap transition when MoS_2 is reduced from multilayer to monolayer (1, 2). These 2D monolayer materials have found a wide range of applications as electronic or optoelectronic devices and are especially attractive as active materials for light emission devices such as quantum emitters (3–6), electroluminescent (EL) devices (7–18), and nanolasers (19–23) due to several favorable optical properties. These properties (24) include strong exciton emission as opposed to electron-hole plasma emission in conventional semiconductors, thinnest gain media for ultralow-power lasers (24), the existence of optical gain at ultralow carrier injection level (25), and flexibility for integration with various substrates and silicon in particular (15, 21, 23, 26). As a result, 2D material–based lasers (19–23) and EL devices (7–18) have been an active topic of research for the past 5 years. However, so far, laser demonstrations have been exclusively based on optical pumping. Despite great efforts in achieving electrical injection emitters, many challenges remain. Further progress has been largely stagnant after the initial work (7–9) due to many challenges of both near-term technical and long-term principle nature.

It is therefore critically important to revisit all key design aspects of an EL device based on 2D materials to assess the near- and long-term challenges and potential solutions. First, ohmic contact remains very difficult to achieve with few rare demonstrations so far (27–29). Contacting 2D materials directly with metallic or conducting layers often leads to notable charge transfer and marked degradation of emission properties. Carrier injections have been demonstrated through the Schottky barriers between monolayer TMDCs and graphene or metals (30) or ohmic contact to monolayer MoS_2 (27, 28), WS_2 (27), and $MoTe_2$ (29), but carrier injection is still not easy. Second, chemical doping techniques well-established in III-V semiconductors for creating p-n junctions are not yet mature enough for monolayer TMDCs. Efforts have been made to create p-n junctions through electrostatic gating (7–9, 15) for carrier injections. However, these electrically gate-controlled p-n junctions lead to complicated structures (7–9, 15) and poor surface utilization of active materials for light emission. Last, 2D materials produced either through direct growth or by exfoliation from bulk are limited presently to fragments or flakes on the order of tens to hundreds of micrometers in sizes (31, 32). These small fragments place a severe limit on the sizes of devices and the long-term scalability of fabrication. While some of these challenges are near term or technical, many of them are intrinsic and long term due to the unique nature of 2D monolayer materials.

To overcome these challenges, we need go beyond the paradigms of conventional semiconductor optoelectronic devices in all these respects. It is interesting to find out whether and how alternative device designs could avoid these existing challenges while taking advantage of the unique features of the new 2D materials. Here, we propose and experimentally demonstrate such an alternative design for EL devices where we need no doping, no ohmic contact, or any electrode contacts with gain layers. We do not require large sizes of flakes of 2D materials, and large devices can be made using small fragments of materials. Our design of EL devices is based on a simple metal-insulator-semiconductor structure, where the metal layer consists of a pair of interdigitated electrodes (IDEs) with hexagonal boron nitride (h-BN) as an insulator and monolayer TMDCs as semiconductors, as schematically shown in Fig. 1 (A to C). We demonstrate that the EL can be achieved by alternating the voltage polarity of the pairs of IDEs. In these devices, preexisting

[1]Department of Electronic Engineering, Tsinghua University, 100084 Beijing, China. [2]Frontier Science Center for Quantum Information, 100084 Beijing, China. [3]Beijing National Research Center for Information Science and Technology, 100084 Beijing, China. [4]School of Electrical, Computer, and Energy Engineering, Arizona State University, Tempe, AZ 85287, USA.
*Corresponding author. Email: cning@tsinghua.edu.cn
†These authors contributed equally to this work.
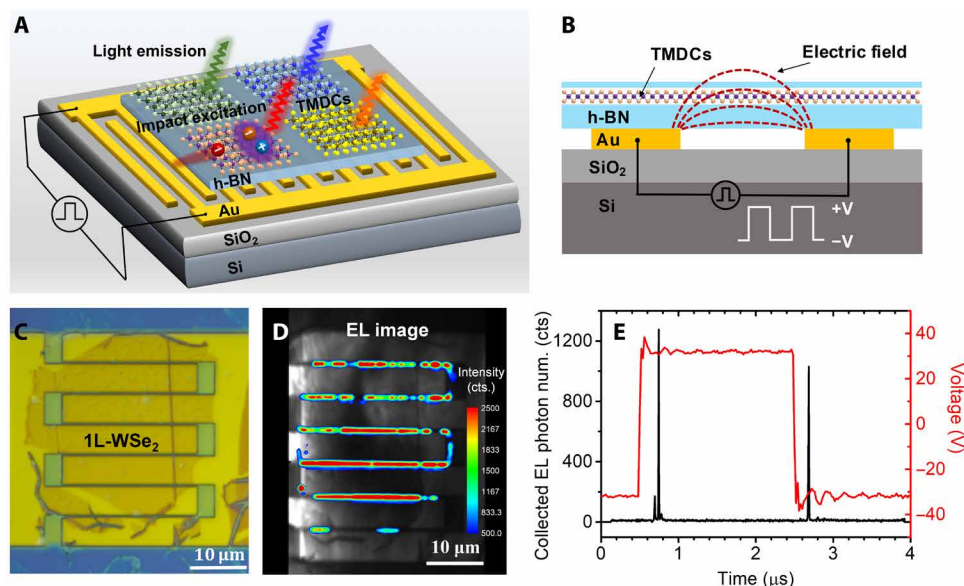
Fig. 1. Device structure and basic properties. (**A**) Schematic diagram of the device, consisting of monolayer TMDCs and a thin h-BN layer of 20 to 50 nm on Au IDEs. (**B**) Cross-sectional view of the device and schematic electric field lines (dark red dashed lines) in the gap between two Au IDEs fingers (yellow). Optical (**C**) and EL (**D**) images of a device with a monolayer (1L) WSe$_2$, respectively. Scale bars, 10 μm. (**E**) EL pulsed emission in time domain and its synchronous square wave voltage applied to the IDEs, with a period of 4 μs and 50% duty cycle. cts, counts.

charges are accelerated by the high local electric fields from IDEs, which then generate excitons through impact excitation, instead of a conventional injection of electrons and holes from electrodes. This alternative device design takes full advantage of the extremely large exciton binding energy (200 to 600 meV) in TMDC materials, leading to a reduced probability of dissociation and increased probability of radiative recombination of impact-generated excitons. Because of many intrinsic advantages of this alternative design, our devices achieved a conversion efficiency (CE) from preexisting carriers to emitted photons of 16% at room temperature. In addition, our approach has the feasibility in using fragmented pieces of materials, and we also demonstrate a multicolor device containing three different TMDC materials.

RESULTS

Our proposed device is shown schematically in Fig. 1A, with the vertical structure shown in Fig. 1B. The device consists of a pair of IDEs as back gates on SiO$_2$/Si substrate. The IDEs are covered first by a layer of h-BN as a dielectric layer before a monolayer of TMDC is transferred, which is then capped by another h-BN layer to prevent the degradation of TMDCs. The transfer of h-BN and TMDCs layers was accomplished through a dry transfer technique (33) (section S1). Note that the insulating h-BN layer between TMDCs and electrodes needs to be thick enough to prevent dielectric breakdown and chosen to be 20 to 50 nm in our devices. In our cases, no dielectric breakdown or tunneling occurs upon AC field application, as shown by the alternating voltage and current characteristics of the device (section S2). The distance between neighboring electrodes is usually in the range of hundreds of nanometers for a strong electric field. Figure 1C shows the optical image of a device using monolayer WSe$_2$ as the active material, with the width of metal fingers and the gap of 5 μm and 400 nm, respectively. The

corresponding EL image of the device at room temperature is shown in Fig. 1D, which is captured by a liquid nitrogen–cooled charge-coupled device (CCD) camera (section S2). The device was driven by a 52-V square wave (B1500A, Keysight), whose polarity is alternating with a period of 100 μs. As seen there, the bright EL from WSe$_2$ mainly appears between the horizontal gaps of the IDE fingers, where a strong in-plane electric field is generated (see Fig. 1B). In addition, there is also weak emission from the vertical edges of the electrodes, where the separation between the IDEs is significantly larger compared to the region of horizontal gaps. This emission is related to the enhanced electric field near the edges of electrodes, as shown in fig. S5B. In addition to the EL image, the pulsed light emission of our device in time domain is shown in Fig. 1E, together with the synchronous square wave voltage that was applied to the IDEs. The voltage between the pair of IDEs switches between +30 and −30 V here, with a period of 4 μs and 50% duty cycle.

Since there is no injection of carriers from the electrode to the TMDCs, yet the light emission occurs in TMDCs that are between the gaps of IDE fingers, the mechanism of light emission deserves scrutiny. The overall physical processes during the device operation are depicted in Fig. 2A. First, most 2D TMDCs contain certain levels of preexisting electrons or holes due to impurities or defects. Under the driving of a strong in-plane electric field, the preexisting carriers are accelerated to acquire high kinetic energies. Then, the collisions of high-energy drifting carriers with lattice (inelastic impact) transfer their energies to valence electrons, generating excitons. These excitons then recombine radiatively to emit light or recombine nonradiatively with a certain probability. Obviously, by this direct electric field driving, the device only emits light in a short burst once. To make the light emission sustained, the polarity of the voltage is reversed so that the carriers could be driven to the reverse direction to generate excitons and light emission. By applying an
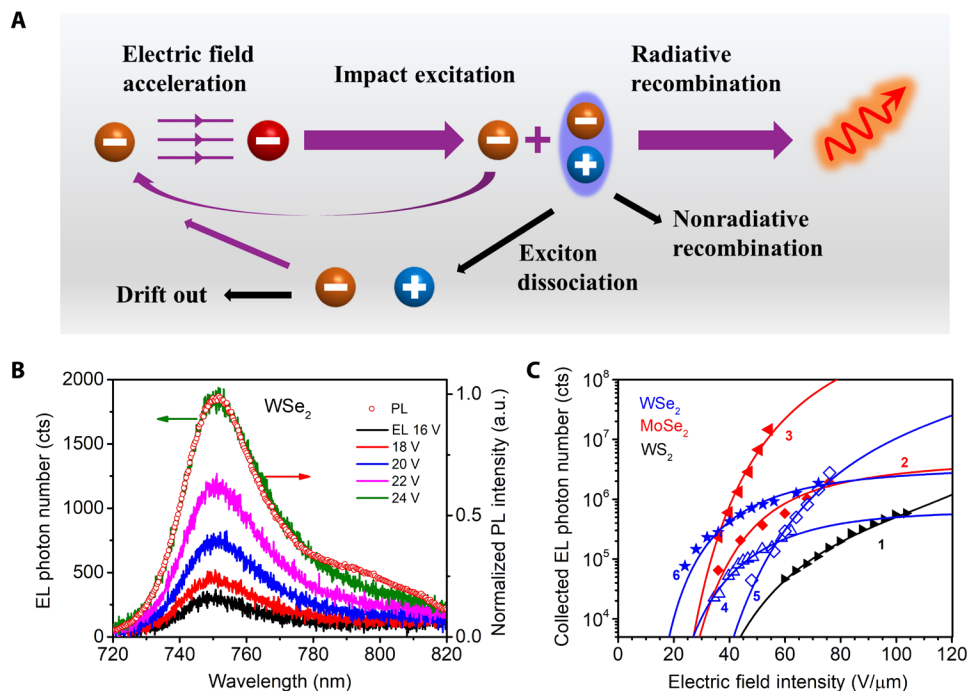
Fig. 2. Mechanism of impact excitation and electrical luminescence. (A) Schematic of the overall physical processes during the device operation under a strong electric field. (**B**) EL spectra of a WSe$_2$-based device under different driving voltages and a PL spectrum pumped by 633-nm laser. a.u., arbitrary units.(**C**) Photon numbers as collected versus electric field for six devices using three different TMDCs. The periods of square wave voltages and integration time for EL spectra capture are listed in table S3.

AC voltage of a given periodicity, the impact excitation and light emission can proceed periodically with two EL pulses produced at the switching edges, as shown in Fig. 1E. The delay time of light pulse after voltage switching is about 200 ns here, which is mostly attributed to the resistance-capacitance effect of IDEs (section S2).

Note that, in addition to the recombination after impact excitation, the excitons can also dissociate in the strong electric field with certain probability. In addition, the electrons and holes from dissociated excitons can participate in the secondary impact excitation to create new excitons or drift outside of the acceleration region. That is, there are two main mechanisms in the strong electric field–driven device, namely, the impact excitation and exciton dissociation. The impact excitation rate (Γ_e) follows the relationship (*34*, *35*) of $\Gamma_e \propto \exp(-F_e/F)$. The critical field ($F_e$) corresponds to the minimal field required to accelerate a charge unit to reach the exciton emission energy (E_x). Because of the requirement of momentum conservation, the electron needs to acquire ~1.5E_x or $e\lambda_m F_e = 1.5E_x$ (*36*), where λ_m is the mean free path of carriers in monolayer TMDCs. Similarly, the exciton dissociation rate (Γ_d) follows a similar relationship, $\Gamma_d \propto \exp(-F_d/F)$. $F_d = E_b/(ed)$, where F_d and E_b are the critical dissociation field and exciton binding energy, respectively, and where d is the exciton Bohr radius. Incidentally, a clear advantage of using TMDCs for impact excitation–based light emitters is the large exciton binding energy. The critical field for the exciton dissociation for the TMDCs is expected to be up to two orders of magnitude larger than for conventional semiconductors. To verify the mechanism of exciton generation and understand the details of physical processes, we model the system by the following coupled rate equations for electrons and excitons (see section S6 for more details)

$$\frac{dN}{dt} = \Gamma_e n - \Gamma_d N - (\gamma_r + \gamma_{nr})N \qquad (1)$$

$$\frac{dn}{dt} = J + \Gamma_d N - \gamma_d n \qquad (2)$$

where N and n are the exciton and free carrier areal density, respectively. Γ_e is the impact excitation rate, Γ_d is the dissociation rate of an exciton, $\gamma_r = 1/\tau_r$ is the exciton radiative recombination rate, $\gamma_{nr} = 1/\tau_{nr}$ is the nonradiative recombination rate, γ_d is the rate for carriers to drift out of impact region, and J is the carrier flux density at which carriers are injected into impact region. By solving the rate equations (section S6), we can theoretically establish the relationship between the collected photon number and the electric field intensity (eq. S10). Meanwhile, we also experimentally measured the light-emitting signals under different driving voltages, so we can verify the model by fitting the experimental results. Figure 2B shows the EL spectra of a WSe$_2$-based device under different voltages with a period of 40 μs and an integration time of 5 s, compared with a normalized photoluminescence (PL) spectrum pumped by a 633-nm continuous wave (CW) laser. The agreement of the EL and PL spectra verifies that the EL from our device originates from the radiative recombination of excitons and trions, as fitted in fig. S3. Figure 2C shows the number of collected photons by the measurement system as a function of electric field intensity for six devices made with three different TMDCs at room temperature. The electric field intensities under different voltages are numerically simulated, as described in section S5. The periods of square wave voltages and integration time for EL spectra captured in measurements are listed in table S3. The solid lines are the fitting results according to the solutions of the rate equations. The fitted values related to the

critical field and other key parameters are listed in table S4. The good agreement between the rate equation results and the experimental results is strong evidence for the exciton generation mechanism by impact excitation. We point out that the other possibility of thermal emission (37) can be safely excluded (see section S7 for detailed explanation).

Figure 3A shows the photon number of EL within a fixed integration time (1 s) and of a single light pulse under different driving frequencies from 1 kHz to 1 MHz. It is clear that when the frequency of driving voltage increases, the generated photon number in a single light pulse decreases monotonically. This is because it takes a minimal length of time for the carriers to be accelerated to the critical impact excitation energy to generate an exciton. This minimal time depends on the sample quality or carrier mobility and, more specifically, on the local field intensity. As shown in the simulation in section S5, the fields directly above the IDEs are much weaker than in the gaps. It therefore takes a much longer time for electrons directly above electrodes to be accelerated to reach high enough energy. This is the principal limitation of device speed. In our devices, the width of electrodes is comparable to that of the gap. Device

A

B

C

Fig. 3. Effects of modulation frequency and switching time. (**A**) EL integrated intensities within a fixed integration time of 1 s (black) and a single pulse (red) as a function of driving frequency for device 3# (MoSe$_2$) with alternating voltage (+30 and −30 V). (**B**) The single light pulses under different voltage switching time in the time domain. (**C**) The integrated intensity (black squares) and width (red circles) of each pulse versus switching time.
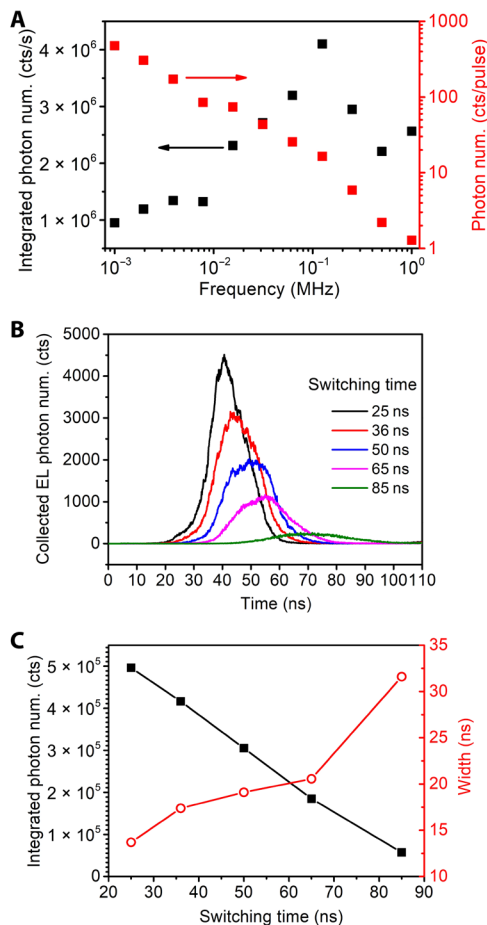
speed can be improved by reducing the width of IDEs in the future. While the generated photon number of a single light pulse decrease, the pulse number within a fixed integration time increase with driving frequency from 1 kHz to 1 MHz. Therefore, the integrated EL intensity per unit time shows a nonmonotonic trend and reaches the highest level around 0.1 MHz. Besides, the switching time (corresponding to the rising and falling edges in Fig. 1E) of driving voltage can significantly affect the light pulses. As shown in Fig. 3B, we zoom in the single pulse in time-resolved measurement under different switching times, from 25 to 85 ns. The device is based on monolayer MoSe$_2$ operating at room temperature. The AC voltage between IDEs is 30 V, with a period of 1 μs. The integration time for each pulse is 100 s. The switching time–dependent integrated intensities and widths of the pulses in Fig. 3B are plotted in Fig. 3C. It is clear that the longer the switching time, the wider the pulse width (Fig. 3C), the lower the peak intensity of the pulse (Fig. 3B), and the lower the integrated intensities of a single light pulse (Fig. 3C). This is because the longer the switching time, the more carriers drift across the IDE gap at low velocity before reaching the critical energy for impact excitation. In our results presented in Fig. 2, the switching time is 40 ns, and it is 25 ns elsewhere that not specifically declared in this paper.

For our injection-free device, CE is defined as the ratio of the number of emitting photons within a single light pulse to the entire preexisting carriers in the material, given as (see eqs. S10 and S11 in section S6)
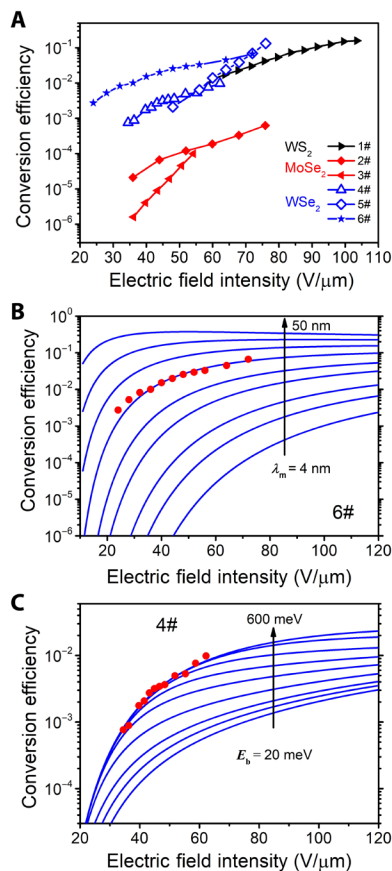
$$CE = \frac{N_{ph0}}{N_c} = \frac{N_{ph}}{\eta \cdot n_{pulse} \cdot n_0 \cdot S} \quad (3)$$

N_{ph0} is the number of the emitted photons in a single pulse, and N_c is the number of preexisting carriers in TMDC materials. $N_c = n_0 S$, where n_0 is the background areal carrier density (measured by the four-probe method in field-effect transistor devices as described in section S8) and S is the area of the monolayer TMDC material on the IDE region. N_{ph} and n_{pulse} are the number of collected photons of our measurement system and the number of light pulses within the integration time, respectively. The detailed calculation for n_{pulse} is shown in section S6. Significantly, η is the overall measurement efficiency of the measurement system, defined as $\eta = \eta_{sys}\eta_{lens}$. η_{sys} is the system transmission efficiency, including the transmission efficiency of the optical system including all optical components such as slit, grating, and Si CCD (see section S4 for details). η_{lens} is the collection efficiency of the lens. We carefully estimated η_{lens} for the emission of in-plane–oriented dipoles in TMDCs for our case by integrating the dipole emission profile over the numerical aperture (NA) of the objective (in section S4, where we also discuss the η_{lens} for isotropic emission and the Lambertian source).

Figure 4A presents the CE determined through Eq. 3 for the same six devices, as presented in Fig. 2C, versus electric field intensity. The parameters needed for CE are listed in table S3, and the values of N_{ph} are taken from Fig. 2C. We see from Fig. 4A that CE increases exponentially with the driving electric field intensity, consistent with the impact excitation mechanism (see section S6). The highest CE of 16% is reached at the field value of 103 V/μm in a WS$_2$ device (1#). This is the highest CE value among all the devices that we tested within the field and voltage applied. Note that the calculation methods of lens collection efficiency in literature are different, which affects the estimation of CE. The lens collection efficiency

Fig. 4. CE of the proposed devices. (**A**) Electric field–dependent CE of the six devices (same as in Fig. 2C) based on monolayer WSe$_2$, MoSe$_2$, and WS$_2$. (**B**) Theoretical CE versus electric field intensity (lines) for different values of the mean free path (λ_m = 4, 5, 6, 8, 10, 14, 20, 30, and 50 nm), with dots representing experimental results, when E_b is 400 meV here. (**C**) Theoretical CE versus electrical field intensity (lines) for different values of exciton binding energy (E_b = 20, 40, 60, 100, 150, 200, 270, 400, and 600 meV), with dots representing the experimental values, where λ_m = 11 nm.

calculation in literature is mostly based on isotropic dipole orientations in 3D space, which corresponds to an isotropic emission pattern. In 2D materials, out-of-plane dipoles (dark excitons) typically emit in a different frequency range from the in-plane dipoles (bright excitons). That is, there are no out-of-plane dipoles in the frequency range of bright-exciton emission that we measured. Collection efficiency of 2D TMDCs should be estimated using emission pattern of dipoles oriented in a 2D plane as we did in section S4. We compared the lens collection efficiencies and the corresponding CE values for the two cases in table S1 (section S4). The lens collection efficiency for 2D oriented dipoles is 0.038 instead of 0.026, estimated on the basis of isotropic dipoles. Accordingly, our CE of 16% becomes 23.3% if we use the isotropic model as commonly used in the literature (*11*, *13*). Details are presented in section S4 and table S1. According to our physical model (see eq. S11), the mean free path (λ_m) of carriers and exciton binding energies (E_b) of TMDC materials are critical parameters that affect CE through exciton impact excitation rate (Γ_e) and dissociation rate (Γ_d). To theoretically study the influence of λ_m and E_b on CE, we plot electric field intensity–dependent

CE based on eq. S11 for different values of λ_m and E_b in Fig. 4 (B and C, respectively). In Fig. 4B, we use the data of device 6# for discussion, where the red dots are obtained by CE = N_{ph0}/N_c and blue curves are based on eq. S11 corresponding to λ_m, ranging from 4 to 50 nm (in the sequence of 4, 5, 6, 8, 10, 14, 20, 30, and 50 nm), while other parameters are fixed as listed in table S3 of device 6#. At present, poor material quality and short λ_m are the main reason for relatively low CE. As the field of 2D TMDCs becomes more mature with better material quality, much higher λ_m and thus higher CE can be expected using our approach. In addition to λ_m, values of CE for different E_b are plotted in Fig. 4C, where device 4# is taken for example. The main advantage of 2D TMDCs compared to the conventional III-V or II-VI semiconductors lies in the large E_b. In conventional semiconductors, where E_b ranges from a few to tens of milli–electron volts, excitons are easily dissociated at zero or small field value at room temperature. As shown in Fig. 4C, an increase in binding energy from 20 to 600 meV (corresponding to that of MoTe$_2$) can lead to more than an order of magnitude increase in CE.

One of the great advantages of our proposed device is that, unlike conventional electrical injection devices, we do not require continuous charge transport over a long distance, which would require high-quality materials with a size of devices. Figure 5A is the dark-field optical image of a device based on monolayer WSe$_2$, which was broken into pieces during the transfer process (refer to fig. S1 for more images), as marked by the white dashed lines. However, the disjoined pieces can still light up simultaneously, as shown in Fig. 5B. This advantage could be very consequential for TMDC materials, since it is still very challenging to produce single-crystal quality TMDC monolayer with sizes more than tens of micrometers either through epitaxial growth or by exfoliation. To demonstrate this advantage, we fabricated an EL device with four disjoint pieces of monolayers of three different TMDCs by the same pair of IDEs, as shown in Fig. 5C. When an alternating voltage is applied to the electrodes, three pieces of monolayer TMDCs light up simultaneously in three wavelengths at 620, 750, and 790 nm, as shown in Fig. 5D, where the emitting patterns were marked by false colors. Such a multiwavelength device emission in a wide wavelength range was also achieved previously on the basis of other materials such as InGaAs/InP nanowire (*38*) but can be fabricated on the basis of TMDCs as readily as a single wavelength one, the significant advantages. Figure 5E shows EL spectra of widely studied TMDCs, including monolayer WS$_2$, MoS$_2$, WSe$_2$, MoSe$_2$, MoTe$_2$, and bilayer MoTe$_2$, with emission wavelengths in the range from 600 to 1200 nm. These visible near-infrared (NIR) devices could be of great importance for many applications. Our approach allows large-area EL devices to be made with fragments of TMDC materials or arbitrarily numbers of various TMDCs.

DISCUSSION
Impact excitation has been used for EL devices in carbon nanotubes (*34*, *35*) with externally injected charges and in AC thin-film devices with ion emission centers (*39–42*). In conventional thin-film devices, carriers can be accelerated in semiconductors or nonsemiconductors through electron tunneling in the strong electric field. In general, carriers are more easily to be accelerated with high kinetic energy in semiconductors than nonsemiconductors. On the other hand, the impact excitation by the high-energy carriers and the subsequent emission can only occur in the discrete luminescent centers embedded
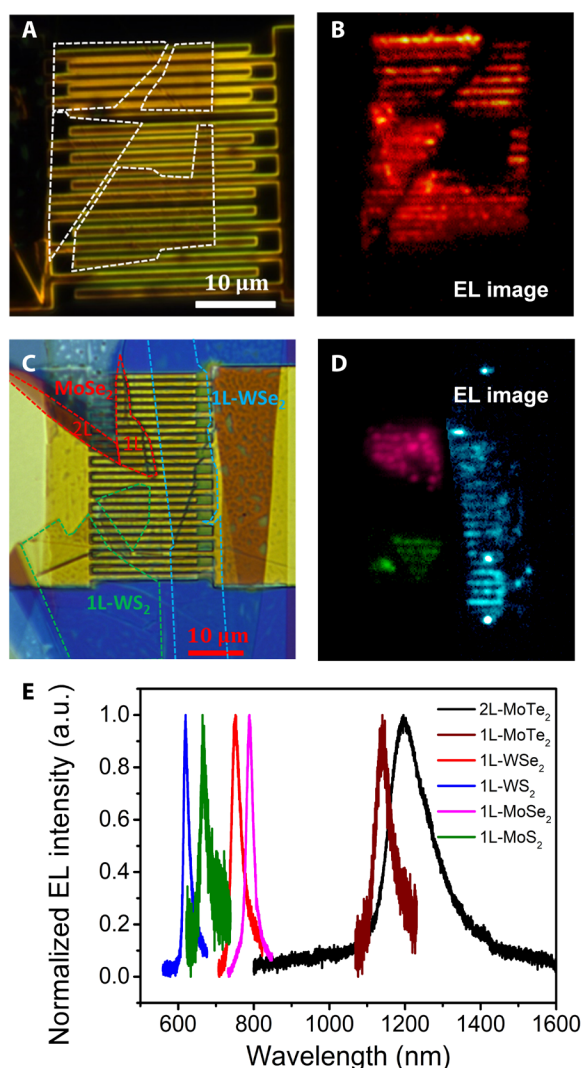
Fig. 5. Multiwavelength device with fragmented pieces of materials. (**A**) Dark-field optical image of a device with disjoint pieces of monolayer WSe$_2$ acting as the active material. (**B**) The light-emitting image of the device in (A). (**C**) Optical image of a device with three different TMDC materials, MoSe$_2$ (red lines), WSe$_2$ (blue lines), and WS$_2$ (green lines). 2L, bilayer. (**D**) EL image of the multicolor device. The false colors mark emissions from different TMDC materials. (**E**) EL spectra of typical semiconductor TMDC materials, including WS$_2$, MoS$_2$, WSe$_2$, MoSe$_2$, and MoTe$_2$.

layered materials that can avoid many challenging issues related to ohmic contact, carrier injection, and charge transfer–related degradation of emitting materials that encountered in current approaches. Excitonic emissions from monolayer TMDC materials span from visible to NIR wavelengths. Our device demonstration can potentially unleash the potential for multicolor or full-color emission for red, green, and blue (RGB) display using three different TMDC materials. All semiconductor RGB displays based on conventional semiconductors are still extremely challenging, despite great progress (*43*). Besides, the repeated light pulses of our devices driven by AC voltage can achieve a frequency up to 1 MHz, which represents enormous potential opportunities in the field of high-speed modulated optoelectronic devices with TMDC materials. This modulation speed can significantly be increased with the improvement of the material quality of TMDCs. High-speed modulation is still a challenging task in TMDC devices, especially for the direct modulation light sources. Furthermore, the CE, a parameter we define for our injection-free EL devices, can reach 16% at room temperature. Last, our design shows better robustness in the fabrication process. The devices still work even if some line defects were introduced during the transfer process. This also shows the feasibility of fabricating large-scale light-emitting devices using only the discontinuous pieces of small-size monolayer TMDC materials. We believe that our approach will greatly facilitate unleashing the tremendous potential of 2D layered materials in device applications for a wide variety of applications.

MATERIALS AND METHODS
Device fabrication
The fabrication process of our devices mainly includes three steps. First, we prepare the IDEs on SiO$_2$/Si substrates through electron beam lithography, electrodes deposition (30/50 nm, Cr/Au), and liftoff. Second, TMDCs and h-BN flakes are mechanically exfoliated from bulk materials (supplier: HQ Graphene and 2D Semiconductors) and covered onto polydimethylsiloxane (PDMS)/glass slide substrates, respectively. The transparent PDMS/glass slide substrates are selected for alignment during the following transfer process. Last, the h-BN flakes and monolayer TMDCs are transferred onto the IDEs by the dry transfer technique. An h-BN flake as an insulating and dielectric layer is firstly transferred onto the IDEs, with the thickness in the range of 20 to 50 nm. Then, the monolayer TMDCs and a cap h-BN flake are vertically stacked by repeating the transfer process. The dry transfer process is carried out on a homemade micromanipulator with a microscope.

PL and EL measurement
The measurement setup for the micro-PL and -EL includes a homemade microscope and a spectrometer equipped with a liquid nitrogen–cooled Si 2D detector and a thermoelectric-cooled InGaAs 2D detector. The PL and EL spectra and EL imaging of the devices based on monolayer WSe$_2$, WS$_2$, MoSe$_2$, and MoS$_2$ are detected by Si detector, while those of the devices based on monolayer and bilayer MoTe$_2$ are detected by InGaAs detector. The PL of monolayer WSe$_2$, WS$_2$, MoSe$_2$, and MoS$_2$ are pumped by a CW semiconductor laser at 532 nm. The PL of MoTe$_2$ is pumped by a CW He-Ne laser at 633 nm. The pumped light is vertically incident onto the sample plane by a ×100 (or ×20) objective with NA = 0.7 (or 0.4), which also collects the emission light. In EL measurements, the

in host materials (e.g., ZnS:Mn, ZnS:CdSe/ZnS quantum dots, etc.) (*39, 41*) for conventional thin-film devices. While in our proposed devices, carriers are accelerated in the monolayer semiconductors, and exciton creation by impact excitation occurs everywhere in monolayer semiconductors rather than some discrete luminescent centers. This means that the monolayer TMDC semiconductors have larger impact excitation cross section, which contributes to a higher impact excitation efficiency in theory.

In summary, we have proposed and demonstrated electric field–induced light emission in monolayer TMDCs at room temperature via applying AC voltage to a pair of IDEs. Instead of conventional carrier injection–based devices, we use the electric field to drive and accelerate charges to achieve impact excitation of excitons for light emission. It is an alternative approach to EL devices based on 2D

devices are driven by AC voltages generated from a semiconductor parameter analyzer (B1500A, Keysight), and the emitting light is collected using the measurement setup mentioned above. The time-resolved light pulses are detected by a time-correlated single-photon counter (TCSPC) integrated into the micro-PL setup. The trigger for TCSPC is also generated from B1500A, having the same frequency and duty cycle (50%) with AC trigger voltage for device operation.

SUPPLEMENTARY MATERIALS

Supplementary material for this article is available at https://science.org/doi/10.1126/sciadv.abl5134

REFERENCES AND NOTES

1. K. F. Mak, C. Lee, J. Hone, J. Shan, T. F. Heinz, Atomically Thin MoS_2: A new direct-gap semiconductor. *Phys. Rev. Lett.* **105**, 136805 (2010).
2. A. Splendiani, L. Sun, Y. Zhang, T. Li, J. Kim, C.-Y. Chim, G. Galli, F. Wang, Emerging photoluminescence in monolayer MoS_2. *Nano Lett.* **10**, 1271–1275 (2010).
3. M. Koperski, K. Nogajewski, A. Arora, V. Cherkez, P. Mallet, J.-Y. Veuillen, J. Marcus, P. Kossacki, M. Potemski, Single photon emitters in exfoliated WSe_2 structures. *Nat. Nanotechnol.* **10**, 503–506 (2015).
4. Y.-M. He, G. Clark, J. R. Schaibley, Y. He, M.-C. Chen, Y.-J. Wei, X. Ding, Q. Zhang, W. Yao, X. Xu, C.-Y. Lu, J.-W. Pan, Single quantum emitters in monolayer semiconductors. *Nat. Nanotechnol.* **10**, 497–502 (2015).
5. C. Chakraborty, L. Kinnischtzke, K. M. Goodfellow, R. Beams, A. N. Vamivakas, Voltage-controlled quantum light from an atomically thin semiconductor. *Nat. Nanotechnol.* **10**, 507–511 (2015).
6. A. Srivastava, M. Sidler, A. V. Allain, D. S. Lembke, A. Kis, A. Imamoğlu, Optically active quantum dots in monolayer WSe_2. *Nat. Nanotechnol.* **10**, 491–496 (2015).
7. B. W. H. Baugher, H. O. H. Churchill, Y. Yang, P. Jarillo-Herrero, Optoelectronic devices based on electrically tunable p-n diodes in a monolayer dichalcogenides. *Nat. Nanotechnol.* **9**, 262–267 (2014).
8. A. Pospischil, M. M. Furchi, T. Mueller, Solar-energy conversion and light emission in an atomic monolayer p-n diode. *Nat. Nanotechnol.* **9**, 257–261 (2014).
9. J. S. Ross, P. Klement, A. M. Jones, N. J. Ghimire, J. Yan, D. G. Mandrus, T. Taniguchi, K. Watanabe, K. Kitamura, W. Yao, D. H. Cobden, X. Xu, Electrically tunable excitonic light-emitting diodes based on monolayer WSe_2 p-n junctions. *Nat. Nanotechnol.* **9**, 268–272 (2014).
10. R. S. Sundaram, M. Engel, A. Lombardo, R. Krupke, A. C. Ferrari, P. Avouris, M. Steiner, Electroluminescence in single layer MoS_2. *Nano Lett.* **13**, 1416–1421 (2013).
11. F. Withers, O. Del Pozo-Zamudio, A. Mishchenko, A. P. Rooney, A. Gholinia, K. Watanabe, T. Taniguchi, S. J. Haigh, A. K. Geim, A. I. Tartakovskii, K. S. Novoselov, Light-emitting diodes by band-structure engineering in van der Waals heterostructures. *Nat. Mater.* **14**, 301–306 (2015).
12. D.-H. Lien, M. Amani, S. B. Desai, G. H. Ahn, K. Han, J.-H. He, J. W. Ager III, M. C. Wu, A. Javey, Large-area and bright pulsed electroluminescence in monolayer semiconductors. *Nat. Commun.* **9**, 1229 (2018).
13. F. Withers, O. Del Pozo-Zamudio, S. Schwarz, S. Dufferwiel, P. M. Walker, T. Godde, A. P. Rooney, A. Gholinia, C. R. Woods, P. Blake, S. J. Haigh, K. Watanabe, T. Taniguchi, I. L. Aleiner, A. K. Geim, V. I. Fal'ko, A. I. Tartakovskii, K. S. Novoselov, WSe_2 light-emitting tunneling transistors with enhanced brightness at room temperature. *Nano Lett.* **15**, 8223–8228 (2015).
14. S. Wang, J. Wang, W. Zhao, F. Giustiniano, L. Chu, I. Verzhbitskiy, J. Zhou Yong, G. Eda, Efficient carrier-to-exciton conversion in field emission tunnel diodes based on MIS-type van der Waals heterostack. *Nano Lett.* **17**, 5156–5162 (2017).
15. Y.-Q. Bie, G. Grosso, M. Heuck, M. M. Furchi, Y. Cao, J. Zheng, D. Bunandar, E. Navarro-Moratalla, L. Zhou, D. K. Efetov, T. Taniguchi, K. Watanabe, J. Kong, D. Englund, P. Jarillo-Herrero, A $MoTe_2$-based light-emitting diode and photodetector for silicon photonic integrated circuits. *Nat. Nanotechnol.* **12**, 1124–1129 (2017).
16. Y. J. Zhang, T. Oka, R. Suzuki, J. T. Ye, Y. Iwasa, Electrically switchable chiral light-emitting transistor. *Science* **344**, 725–728 (2014).
17. Y. Zhu, Z. Li, L. Zhang, B. Wang, Z. Luo, J. Long, J. Yang, L. Fu, Y. Lu, High-efficiency monolayer molybdenum ditelluride light-emitting diode and photodetector. *ACS Appl. Mater. Interfaces* **10**, 43291–43298 (2018).
18. J. Cho, M. Amani, D.-H. Lien, H. Kim, M. Yeh, V. Wang, C. Tan, A. Javey, Centimeter-scale and visible wavelength monolayer light-emitting devices. *Adv. Funct. Mater.* **30**, 1907941 (2020).
19. S. Wu, S. Buckley, J. R. Schaibley, L. Feng, J. Yan, D. G. Mandrus, F. Hatami, W. Yao, J. Vučković, A. Majumdar, X. Xu, Monolayer semiconductor nanocavity lasers with ultralow thresholds. *Nature* **520**, 69–72 (2015).
20. Y. Ye, Z. J. Wong, X. Lu, X. Ni, H. Zhu, X. Chen, Y. Wang, X. Zhang, Monolayer excitonic laser. *Nat. Photonics* **9**, 733–737 (2015).
21. Y. Li, J. Zhang, D. Huang, H. Sun, F. Fan, J. Feng, Z. Wang, C. Z. Ning, Room-temperature continuous-wave lasing from monolayer molybdenum ditelluride integrated with a silicon nanobeam cavity. *Nat. Nanotechnol.* **12**, 987–992 (2017).
22. E. Y. Paik, L. Zhang, G. W. Burg, R. Gogna, E. Tutuc, H. Deng, Interlayer exciton laser of extended spatial coherence in atomically thin heterostructures. *Nature* **576**, 80–84 (2019).
23. Y. Liu, H. Fang, A. Rasmita, Y. Zhou, J. Li, T. Yu, Q. Xiong, N. Zheludev, J. Liu, W. Gao, Room temperature nanocavity laser with interlayer excitons in 2D heterostructures. *Sci. Adv.* **5**, eaav4506 (2019).
24. C.-Z. Ning, Semiconductor nanolasers and the size-energy-efficiency challenge: A review. *Adv. Photonics* **1**, 014002 (2019).
25. Z. Wang, H. Sun, Q. Zhang, J. Feng, J. Zhang, Y. Li, C.-Z. Ning, Excitonic complexes and optical gain in two-dimensional molybdenum ditelluride well below the Mott transition. *Light Sci. Appl.* **9**, 39 (2020).
26. H. Fang, J. Liu, H. Li, L. Zhou, L. Liu, J. Li, X. Wang, T. F. Krauss, Y. Wang, 1305 nm few-layer $MoTe_2$-on-silicon laser-like emission. *Laser Photonics Rev.* **12**, 1800015 (2018).
27. M. H. D. Guimarães, H. Gao, Y. Han, K. Kang, S. Xie, C.-J. Kim, D. A. Muller, D. C. Ralph, J. Park, Atomically thin ohmic edge contacts between two-dimensional materials. *ACS Nano* **10**, 6392–6399 (2016).
28. X. Cui, E.-M. Shih, L. A. Jauregui, S. H. Chae, Y. D. Kim, B. Li, D. Seo, K. Pistunova, J. Yin, J.-H. Park, H.-J. Choi, Y. H. Lee, K. Watanabe, T. Taniguchi, P. Kim, C. R. Dean, J. C. Hone, Low-temperature ohmic contact to monolayer MoS_2 by van der Waals bonded Co/h-BN electrodes. *Nano Lett.* **17**, 4781–4786 (2017).
29. S. Cho, S. Kim, J. H. Kim, J. Zhao, J. Seok, D. H. Keum, J. Baik, D.-H. Choe, K. J. Chang, K. Suenaga, S. W. Kim, Y. H. Lee, H. Yang, Phase patterning for ohmic homojunction contact in $MoTe_2$. *Science* **349**, 625–628 (2015).
30. A. Allain, J. Kang, K. Banerjee, A. Kis, Electrical contacts to two-dimensional semiconductors. *Nat. Mater.* **14**, 1195–1205 (2015).
31. H. Li, G. Lu, Y. Wang, Z. Yin, C. Cong, Q. He, L. Wang, F. Ding, T. Yu, H. Zhang, Mechanical exfoliation and characterization of single- and few-layer nanosheets of WSe_2, TaS_2, and $TaSe_2$. *Small* **9**, 1974–1981 (2013).
32. Y. Zhan, Z. Liu, S. Najmaei, P. M. Ajayan, J. Lou, Large-area vapor-phase growth and characterization of MoS_2 atomic layers on a SiO_2 substrate. *Small* **8**, 966–971 (2012).
33. A. Castellanos-Gomez, M. Buscema, R. Molenaar, V. Singh, L. Janssen, H. S. J. van der Zant, G. A. Steele, Deterministic transfer of two-dimensional materials by all-dry viscoelastic stamping. *2D Mater.* **1**, 011002 (2014).
34. J. Chen, V. Perebeinos, M. Freitag, J. Tsang, Q. Fu, J. Liu, P. Avouris, Bright infrared emission from electrically induced excitons in carbon nanotubes. *Science* **310**, 1171–1174 (2005).
35. V. Perebeinos, P. Avouris, Impact excitation by hot carriers in carbon nanotubes. *Phys. Rev. B* **74**, 121410 (2006).
36. Y. Okuto, C. R. Crowell, Energy-conservation considerations in the characterization of impact ionization in semiconductors. *Phys. Rev. B* **6**, 3076–3081 (1972).
37. L. Dobusch, S. Schuler, V. Perebeinos, T. Mueller, Thermal light emission from monolayer MoS_2. *Adv. Mater.* **29**, 1701304 (2017).
38. I. Yang, Z. Li, J. Wong-Leung, Y. Zhu, Z. Li, N. Gagrani, L. Li, M. N. Lockrey, H. Nguyen, Y. Lu, H. H. Tan, C. Jagadish, L. Fu, Multiwavelength single nanowire InGaAs/InP quantum well light-emitting diodes. *Nano Lett.* **19**, 3821–3829 (2019).
39. V. Wood, J. E. Halpert, M. J. Panzer, M. G. Bawendi, V. Bulović, Alternating current driven electroluminescence from ZnSe/ZnS:Mn/ZnS nanocrystals. *Nano Lett.* **9**, 2367–2371 (2009).
40. J. Benoit, C. Barthou, P. Benalloul, K. Polamo, The electro-optical behavior of SrS:Ce electroluminescent devices under photonic excitation. *J. Appl. Phys.* **87**, 198–202 (2000).
41. D. Bozyigit, V. Wood, Y. Shirasaki, V. Bulovic, Study of field driven electroluminescence in colloidal quantum dot solids. *J. Appl. Phys.* **111**, 113701 (2012).
42. L. Wang, L. Xiao, H. Gu, H. Sun, Advances in alternating current electroluminescent devices. *Adv. Opt. Mater.* **7**, 1801154 (2019).
43. F. Fan, S. Turkdogan, Z. Liu, D. Shelhammer, C. Z. Ning, A monolithic white laser. *Nat. Nanotechnol.* **10**, 796–803 (2015).
44. I. Fushman, D. Englund, J. Vučković, Coupling of PbS quantum dots to photonic crystal cavities at room temperature. *Appl. Phys. Lett.* **87**, 241102 (2005).
45. J. D. Jackson, *Classical Electrodynamics Third Edition* (Wiley, ed. 3, 1998).
46. M. Massicotte, F. Vialla, P. Schmidt, M. B. Lundeberg, S. Latini, S. Haastrup, M. Danovich, D. Davydovskaya, K. Watanabe, T. Taniguchi, V. I. Fal'ko, K. S. Thygesen, T. G. Pedersen, F. H. L. Koppens, Dissociation of two-dimensional excitons in monolayer WSe_2. *Nat. Commun.* **9**, 1633 (2018).
47. T. Brumme, M. Calandra, F. Mauri, Determination of scattering time and of valley occupation in transition-metal dichalcogenides doped by field effect. *Phys. Rev. B* **93**, 081407 (2016).

48. M. Amani, P. Taheri, R. Addou, G. H. Ahn, D. Kiriya, D.-H. Lien, J. W. Ager, R. M. Wallace, A. Javey, Recombination kinetics and effects of superacid treatment in sulfur- and selenium-based transition metal dichalcogenides. *Nano Lett.* **16**, 2786–2791 (2016).

49. V. Podzorov, M. E. Gershenson, C. Kloc, R. Zeis, E. Bucher, High-mobility field-effect transistors based on transition metal dichalcogenides. *Appl. Phys. Lett.* **84**, 3301–3303 (2004).

50. H. I. Jeong, S. Park, H. I. Yang, W. Choi, Electrical properties of $MoSe_2$ metal-oxide-semiconductor capacitors. *Mater. Lett.* **253**, 209–212 (2019).

51. S.-L. Li, K. Tsukagoshi, E. Orgiu, P. Samorì, Charge transport and mobility engineering in two-dimensional transition metal chalcogenide semiconductors. *Chem. Soc. Rev.* **45**, 118–151 (2015).